Chapter 3

The Imaging Survey

The main conclusions of this work are derived from an optical (0.5-1 μm) and near-infrared (1-2 μm) imaging survey of fields centered on the sample of young, massive, isolated Ae/Be stars given in Table 2.1. Our program was designed to enable analysis both of the large-scale star-forming environments (through wide-field optical imaging), and of the stellar populations which are partially - to - completely embedded within the molecular cores (through deep infrared imaging). In this Chapter we describe the data acquisition and processing, the photometric reduction, the survey sensitivity, and the basic image morphologies. In the following Chapter we discuss our optical classification - resolution spectroscopic survey, which is based on the results of the imaging survey. In subsequent Chapters we present the evidence for clusters of young stars associated with Ae/Be stars, analyze the nature of these newly discovered sources.

3.1 Data Acquisition, Processing, and Reduction

3.1.1 Optical Imaging and Photometry

VR_CI_C CCD images were obtained by LAH and S. Strom with the T2KA CCD at the Kitt Peak National Observatory (KPNO) 0.9m telescope in 1993 January under photometric sky conditions. Additional data with the same instrument and telescope were obtained in 1993 August during the trial period of KPNO-staffed "queue" data acquisition. The platescale of these images is 0.69 arcsec pixel^{-1} and

the angular coverage is approximately 23 x 23 arcmin. At VR_CI_C, the "long" exposures were 500 seconds and the "short" exposures were 5 seconds.

The data were processed by subtracting the CCD bias level and dividing by the normalized flat-field appropriate for each wavelength. Flat-field frames were constructed from a median-filtered series of exposures of the "Lesser White Spot" located inside the 0.9m dome.

Stellar sources were initially identified on the I_C frames using a 10σ detection threshold with the DAOFIND algorithm. Following the examination of individual sources on the images, our initial source lists were modified slightly in some cases. Photometry was extracted using the photometry packages in IRAF with a typical aperture radii of 3.5-10 pixels (dependent on the stellar image FWHM) and background values computed from the median number of counts over sky annuli of, typically, 20 pixels. Corrections for the difference in source counts between the smaller aperture used to measure the program stars (chosen to maximize signal-to-noise) and the 15 arcsec aperture used to measure standard stars (chosen to include the wings of the stellar intensity profile) were determined as averages from isolated stars on the data frames themselves. In regions where source crowding was thought to influence the photometry, local point-spread function fitting was done. In general the final photometry was taken from the long exposures, except in cases of source saturation in which the short exposures were used. The data were calibrated on the Cousins photometric system using the standard fields of Landolt (1992). The standards span the range of colors expected to characterize our target objects $(V - R_C) \approx (R_C - I_C) \lesssim 1.2$; no color terms were necessary in our transformation equations.

3.1.2 Infrared Imaging and Photometry

Infrared images were acquired with two different cameras – the University of Massachusetts NICMASS camera and the KPNO SQIID camera.

With a NICMOS-3 array mounted in the NICMASS camera (see Skrutskie *et al.* 1995 for a full description of the instrument), JHK$_S$ images were obtained by LAH, M. Meyer, and P. Knezek in 1993 March, 1993 September, 1994 February, and 1994 May at the Michigan-Dartmouth-MIT 2.4m and 1.3m telescopes. During the first two of these runs the array was of engineering-grade array but was upgraded to a science-grade array following the 1993 September run. The warm optics configuation of the NICMASS dewar yields a platescale which varies from run-to-run, between 0.43 and 0.50 arcsec pixel^{-1} on the 2.4m telescope and between 0.81 and 0.82 arcsec pixel^{-1} on the 1.3m telescope at K$_S$ for these particular sets of observations. The field sizes also vary from run-to-run and are dependent on our mapping technique; they range between regions from about 1 - 5 arcmin on a side. While the J,H filters in the NICMASS camera are typical, the K$_S$ filter is "special" in that with a bandpass of 2.02 - 2.32 μmit is narrower and slightly bluer than the usual K filter. Colors quoted in the natural NICMASS system match those in the standard CIT system at the 10% level in $(J-H)$ and at the 5% level in $(H-K)$. The exposure times were dependent upon the background level, which of course changed from night - to - night and from run - to - run. Once set to the maxima possible K$_S$, though, the total integration times were scaled at H and J to go deeper in magnitude at shorter wavelengths, in an attempt to obtain data which was "complete" to roughly the same visual extinction at J, H, and K$_s$. In general we were successful with this approach and in some cases even detect sources at J which we do not detect at K!

With a set of PtSi arrays mounted in the SQIID camera (see Ellis *et al.* 1992 for a full description of the instrument), JHK images were obtained with the

KPNO 1.3m telescope in 1991 by K. Merrill and I. Gatley, in 1992 January by S. Strom and K. Strom, and in 1992 December by LAH and S. Strom. The combination of detector response as a function of wavelength and specially designed filters, yields a photometric system for SQIID which is easily transformable to the CIT system (Elias *et al.* 1982). For the set of data provided by Merrill *et al.* , SQIID still contained engineering-grade arrays with some cosmetic defects, which were most evident in the K channel; subsequent observing runs made use of science-grade arrays. At JHK, the "long" exposures were 180 seconds and the "short" exposures were 5 seconds.

All of the infrared data were acquired using a gridding technique. For the NICMASS observations, overlapping frames offset by 20-40 arcsec at each step, were taken over 4-8 positions covering the central stellar group. This method provides maximum sensitivity over approximately 90% of the field. For the SQIID observations, dithered pairs of images offset from each other by 20 arsec in right ascension, were taken on 50 arcsec grid centers, providing an overlap between adjacent exposure pairs of approximately 20 percent of the size of the array. The method of dithered pair observations allows for bad-pixel masking without any loss of data, while sufficient grid overlap assures proper spatial registration and background intensity matching among the individual images.

For both the NICMASS and the SQIID data, individual frames were processed by first subtracting a median-filtered sky frame, constructed from "off-field" exposures taken at each wavelength near-in-time to the source observations, and then dividing by a flat-field frame, constructed by normalizing the median-filtered sky exposures. Final composite images are constructed by performing 1) a linear geometrical transformation based on the positional matching of single stars appearing on multiple images, followed by 2) an intensity registration to correct the indeterminate background level created during sky subtraction and flat

fielding. For NICMASS, this is accomplished separately for each bandpass by shifting the individual frames to a common grid position and scaling them by the median value of all pixels in the overlap region between frames. The relative linear geometric transformation (offset, rotation, and magnification) between wavelength channels is determined using stars on the final mosaics themselves. For SQIID, first an overlapping grid of single frames from one bandpass channel are registered pairwise using stars within their common overlap region and then the second element of each dithered pair is registered to its mate using stars common to both. Since the images at all three wavelengths are taken simultaneously, spatial registration at any one wavelength implicitly registers the others. The relative linear geometric transformation (offset, rotation, and magnification) between wavelength channels is determined from independent observations of globular clusters and the JHK frames are geometrically transformed to lie atop one another before combining. During final image combination, each frame is masked for bad pixels, shifted linearly in X and Y, and intensity offset by a constant calculated according to the median value of all pixels in the overlap region between it and each of its neighboring frames. Careful comparison of photometry performed on individual and composite images reveals that neither the modest linear geometric transformations nor the intensity offsetting have any significant effect on the photometry.

Stellar sources were initially identified on the K frames using a 10σ detection threshold with the DAOFIND algorithm. Initial source lists were modified slightly following the examination of individual sources on the images. Photometry at J, H, and K was extracted using the APPHOT and DAOPHOT photometry packages in IRAF. Aperture and sky radii were frame-dependent, but were typically chosen to have between 3-7 pixels diameter apertures with the sky contributions determined from the median values of pixels in radial annuli

approximately 15 pixels in width. Aperture photometry was usually sufficient, but in the cases of extreme crowding and/or highly variable nebular background, we employed the method of constructing a point spread function from a set of relatively isolated, intermediate brightness stars on each mosaiced image, and fitting this point spread function to the sources. The data were calibrated on the CIT photometric system using the standards of Casali (1992), which were first transformed from the UKIRT system to the CIT system (NICMASS observations), or Elias (1982) (SQIID observations).

3.1.3 Astrometry

Astrometry was derived in the astrometric system defining the Hubble Space Telescope Guide Star Catalog (GSC) using the IRAF tasks TFINDER and TASTROM. We first calibrated the large-field CCD frames to the GSC system and then used the derived solutions to calibrate the smaller infrared frames. The standard deviations per point for our astrometry are typically around 0.3 arcsec rms, but can be slightly worse (up to 0.5 arcsec) in regions which sample the intersection of multiple GSC plates.

3.2 Survey Sensitivity to Pre-Main Sequence Stellar Populations

The photometric results derived from our imaging data are presented as needed in subsequent Chapters. Of general interest at the present time, however, are the observational completeness limits and their translation into physical units (stellar mass, age, and extinction). We assess these limits by transforming the D'Antona & Mazitelli (1994) pre-main sequence tracks (computed with the Alexander - CM opacity - convection prescription) into the various observational planes. We discuss the optical and the infrared limits in succession.

For the optical frames, completeness limits were roughly determined (to an accuracy of 0.2 mag) by constructing a histogram of the magnitudes derived for all

sources detected over our entire 23 x 23 arcmin fields, at a level of 10σ or above. This method assumes that the fraction of the field over which there is significant molecular core extinction is small, and thus that the source counts at the faint end are dominated by stars randomly distributed in distance along a line - of - sight though the Galaxy. This method is more direct, but perhaps less accurate, than adding artificial stars of sequentially decreasing brightness to the frames and attempting to recover them, as we will do for the infrared images. The sense of the inaccuracy is that for the optical frames we could be underestimating our completeness limits. We quote "completeness" as the magnitude at which the shape of the source count distribution with magnitude begins to flatten, $V \approx R_C \approx 18.75$ mag and $I_C \approx 18.25$ mag typically, with the faintest detectable sources about 2 magnitudes fainter. As the telescope, instrument, and integration times for all of our CCD data are the same, the quoted completeness limits apply equally to all regions in our sample, to within a few tenths of a magnitude.

For the infrared frames, completeness limits were derived empirically. We used the ADDSTAR routine in IRAF to add test stars into the frames and then the DAOFIND routine to determine what fraction of these artificial stars were recoverable as a function of magnitude. The faintest detectable sources are typically 2 mag fainter than the completeness limits. We estimate the 10σ completeness (recovery of 100% of the artificial sources using a 10σ threshold) limits for our most sensitive frames, the 2.4m MDM/NICMASS observations, to be K = 15.3 mag, H = 17.8 mag, J = 18.8 mag. To first order, these numbers can be scaled by the relative integration times and telescope diameters, to obtain rough completeness limits for slightly less sensitive data acquired with the same instrument. We will return to the issue of relative completeness in Chapter 5 when we investigate differences in K-band sensitivity between our heterogeneous set of images for different Ae/Be regions. For now, we note that as we intentionally

acquired the NICMASS data by scaling relative JHK$_S$ integration times to be more sensitive at shorter wavelengths (so as to be "complete" to the same extinction limits); thus any source detected at K$_S$ is also detected at H and J in the range of colors expected to characterize our sources. For the less-sensitive 1.3m KPNO/SQIID frames, our completeness is typically to K = 13.5 mag, H = 14.5 mag, J = 16.0 mag.

At this point we divide our discussion into two parts. First, we compute monochromatic completeness limits at I$_C$-band and K-band (the reddest bandpasses of our optical and infrared surveys, respectively), which we use in estimating our sensitivity to various populations from simple source counts at these wavelengths. Second, we investigate completeness in color-magnitude diagrams, which we use to deredden optical and infrared sources to determine intrinsic stellar properties.

We report physical monochromatic completeness limits based on photometric completeness levels of I$_C$= 18.3 and K=15.3, in Tables 3.1 and 3.2 for distance moduli corresponding to 500 and 1000 pc (our program sources are found over a range of distances from 440-1300 pc). Although these limits do not strictly apply to every region in our survey, we feel they are representative of our sensitivity levels. As can be seen from a comparison of these two tables (for example by tracing the location of a 0.1 M$_\odot$ star through the grid of stellar age and source extinction), we are significantly more sensitive in the infrared to heavily extincted low-mass stars than we are in even the deepest optical frames available to us. The power of a deep infrared photometric survey will become even more clear in the following discussion of completeness in color-magnitude diagrams.

Because we intend to use our photometric survey as the basis not only for identifying sources physically associated with young Ae/Be stars, but also for investigating the nature of these sources, we must discuss our survey sensitivity as

Table 3.1.
Mass Sensitivity Limits for
Completeness to I_C = 18.3 mag

d = 1000 pc

	A_V = 1 mag	A_V = 2 mag	A_V = 5 mag
10^5 yr	<0.08 $M_\odot$	0.11 $M_\odot$	0.18 $M_\odot$
10^6 yr	0.10 $M_\odot$	0.12 $M_\odot$	0.33 $M_\odot$
3×10^6 yr	0.15 $M_\odot$	0.20 $M_\odot$	0.60 $M_\odot$
10^7 yr	0.23 $M_\odot$	0.30 $M_\odot$	0.90 $M_\odot$

d = 500 pc

	A_V = 1 mag	A_V = 2 mag	A_V = 5 mag
10^5 yr	< 0.08 $M_\odot$	< 0.08 $M_\odot$	< 0.08 $M_\odot$
10^6 yr	< 0.08 $M_\odot$	< 0.08 $M_\odot$	0.10 $M_\odot$
3×10^6 yr	< 0.08 $M_\odot$	< 0.08 $M_\odot$	0.14 $M_\odot$
10^7 yr	0.11 $M_\odot$	0.13 $M_\odot$	0.22 $M_\odot$

Table 3.2.
Mass Sensitivity Limits for
Completeness to K = 15.3 mag

d = 1000 pc

	A_V = 5 mag	A_V = 10 mag	A_V = 20 mag
10^5 yr	<0.08 $M_\odot$	0.08 $M_\odot$	0.15 $M_\odot$
10^6 yr	0.10 $M_\odot$	0.12 $M_\odot$	0.40 $M_\odot$
3×10^6 yr	0.25 $M_\odot$	0.35 $M_\odot$	0.75 $M_\odot$
10^7 yr	0.38 $M_\odot$	0.50 $M_\odot$	1.00 $M_\odot$

d = 500 pc

	A_V = 5 mag	A_V = 10 mag	A_V = 20 mag
10^5 yr	< 0.08 $M_\odot$	< 0.08 $M_\odot$	< 0.08 $M_\odot$
10^6 yr	< 0.08 $M_\odot$	< 0.08 $M_\odot$	< 0.08 $M_\odot$
3×10^6 yr	< 0.08 $M_\odot$	< 0.08 $M_\odot$	0.25 $M_\odot$
10^7 yr	0.12 $M_\odot$	0.20 $M_\odot$	0.38 $M_\odot$

a function of color. Specifically, we generalize our discussion of completeness levels for all regions, in the $I_C - (R_C - I_C)$ and the $J - (J - H)$ color-magnitude diagrams. We will use $(R_C - I_C)$ colors to compute reddening values and I_C magnitudes to compute luminosities, in constructing HR diagrams in Chapter 8. Similarly, we will use the $J - (J - H)$ plane [1] to deredden embedded stellar sources in Chapter 7, and estimate their ages and masses.

In Figures 3.1 and 3.2 we translate the pre-main sequence evolutionary mass tracks and age isochrones into these color-magnitude planes for distance moduli corresponding to 500 and 1000pc. For nearby regions, deep R-,I-band imaging can detect unreddened young ($\tau < 3$ Myr) stars of all masses. Stars which are reddened from their intrinsic locations with mass and age in this diagram, however, move along the indicated reddening vector, and may fall below the photometric completeness limits. Thus in the presence of any appreciable extinction (as is implied towards the Ae/Be regions in this study from derived molecular column densities), young sub-solar mass objects are missed and we must go to the near-infrared in order to uncover these populations. In the infrared, our J,H photometry extends faint enough to be sensitive to stars of all masses down to the hydrogen burning limit (0.08 $M_\odot$), for a given age and a given visual extinction. As an example, for a source at 1000 pc observed with our longest integration time with NICMASS on a 2.4m telescope (*e. g.* the BD +40° 4124 region), the depth to which we can probe a 10 Myr old stellar population corresponds to $A_V \approx 10$ for 0.1 $M_\odot$ stars and $A_V \approx 40$ for 10 $M_\odot$ stars. Younger stars are more luminous, and our completeness as a function of mass and A_V is deeper than the numbers given above.

[1] We employ the $J-(J-H)$ diagram instead of the more traditional $K-(H-K)$ diagram in our infrared color-magnitude diagram analysis, in order to minimize the effects of circumstellar excess flux, which is expected to be prevalent in young stellar objects and to be a greater influence at longer infrared wavelengths.

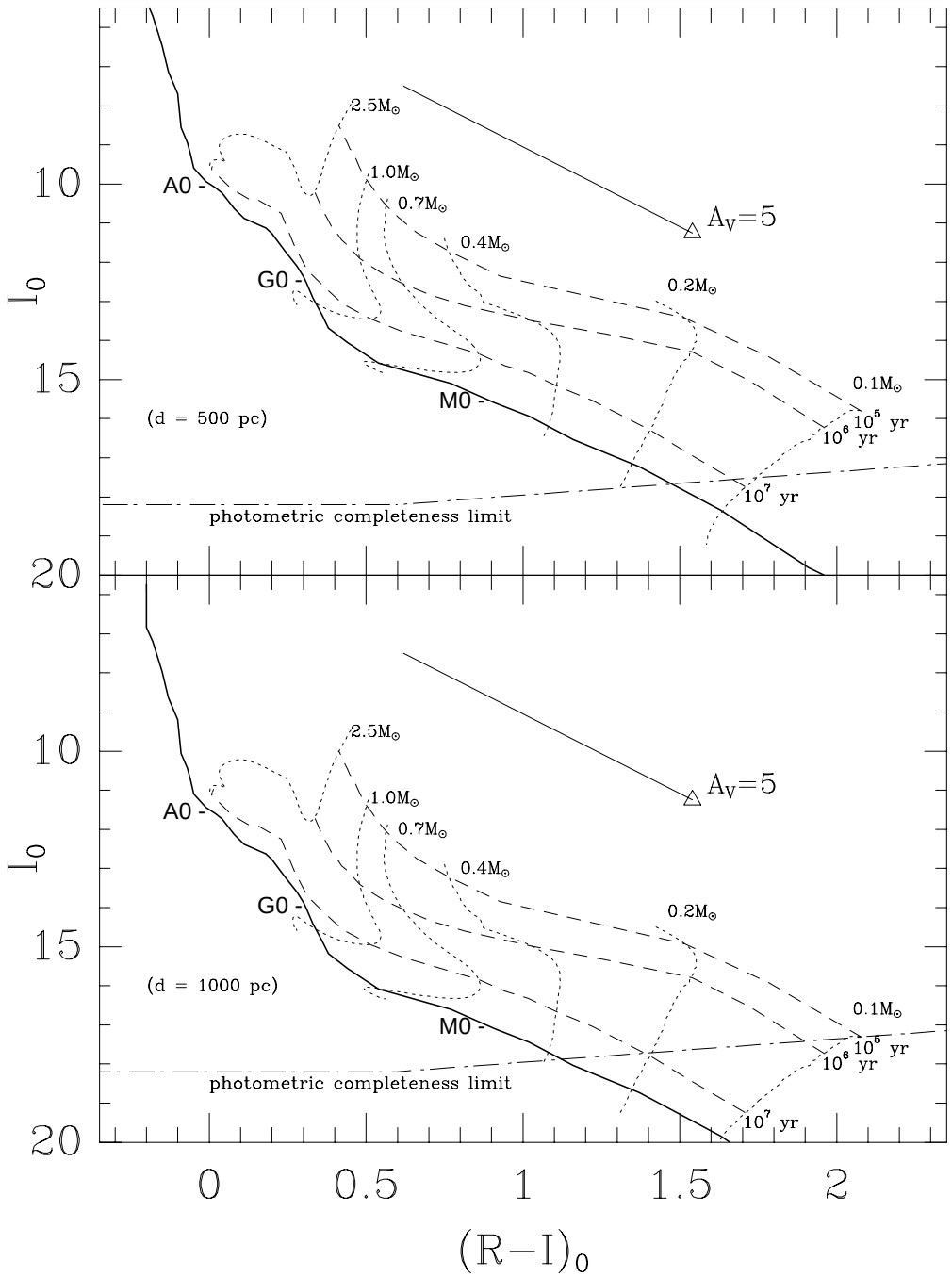

Figure 3.1. *Representative (with source distance) completeness limits for the optical survey.* This figure shows the transformation of our photometric completeness limits into physical completeness limits with mass, age, and extinction for distances of 1 kpc(lower panel) and 0.5 kpc(top panel). As all of our optical data was taken with the same telescope and instrumental setup, the image depth is the same for every region. Although deep R-,I-band imaging can detect nearby young stars of all masses, at large distances or in appreciable extinction, we must go to the near-infrared in order to uncover and investigate young sub-solar mass objects.

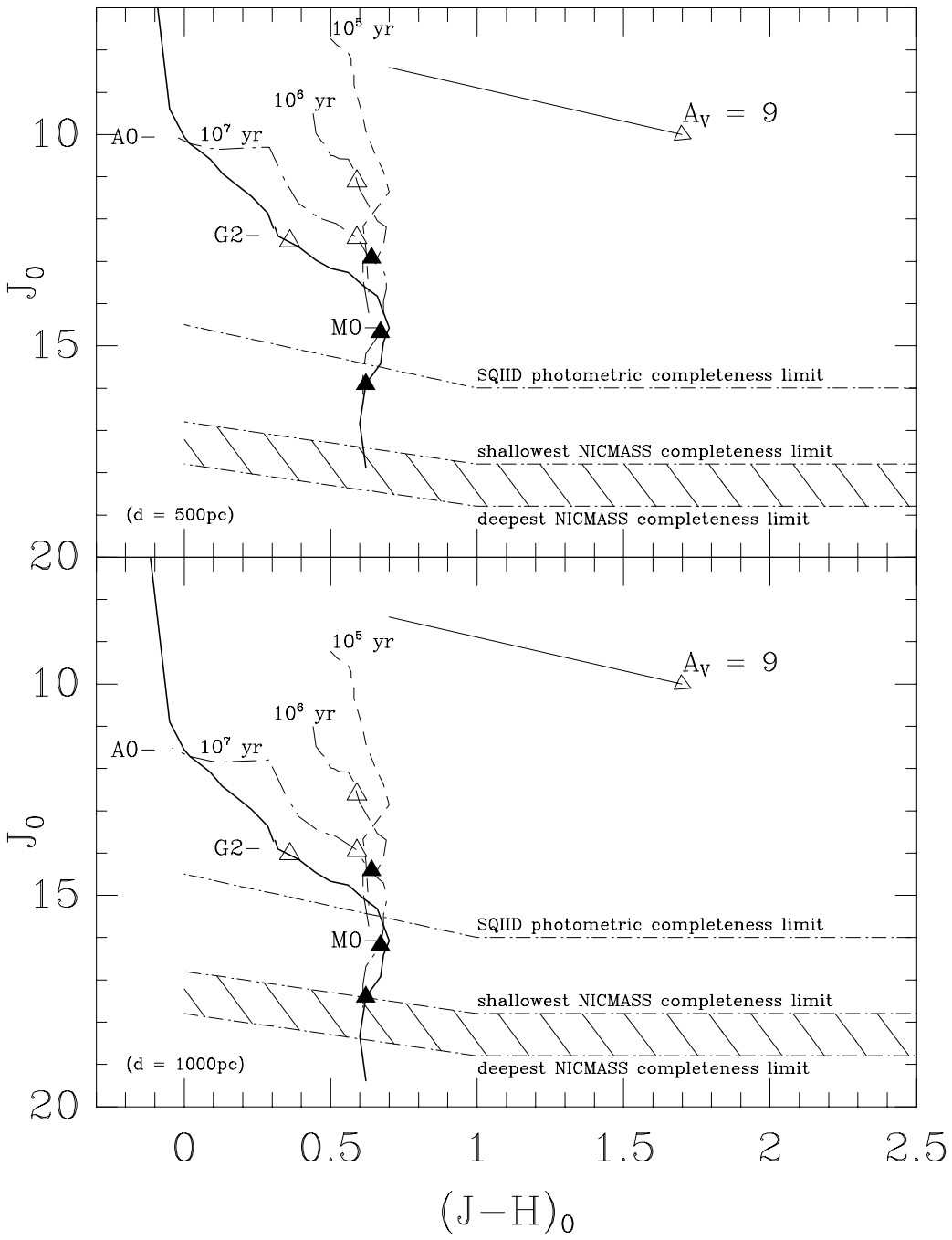

Figure 3.2. *Representative (with source distance) completeness limits for the infrared surveys.* This figure shows the transformation of our photometric completeness limits into physical completeness limits with mass, age, and extinction for distances of 1 kpc(lower panel) and 0.5 kpc(top panel). Mass tracks are not shown explicitly, although the evolution of 0.3 $M_\odot$ (filled triangles) and 1.0 $M_\odot$ (open triangles) stars at 10^6, 10^7, and 10^8 years is as shown. As all of our infrared data was not taken with the same telescope / instrument combination, completeness varies between sources. The upper limit is typical of our SQIID images, while our NICMASS images have a range of completeness limits extending over the shaded region.

In summary, while in the ideal case our optical and infrared surveys would have been conducted for each Ae/Be site to the same limits in mass, age, and extinction (as well as over the same physical area in pc^2), there are inevitable differences in sensitivity between the data sets. We have discused quantitative monochromatic sensitivity limits (Tables 3.1 and 3.2) as well as qualitative color-magnitude diagram limits for images we consider to be typical of those in our survey. We will compute the relative sensitivity numbers for individual regions in Chapter 5, but anticipate our results by stating that in most regions we are sensitive to stellar populations with masses greater than 0.1 $M_\odot$ as long as they are younger than 3 Myr of age and obscured by less than 10 mag of visual extinction.

3.3 General Morphology of the Ae/Be Star Formation Sites

We offer in this section a general description (based on our imaging work) of the local stellar environments in isolated cloud cores containing young, massive Ae/Be stars.

From our large-format optical frames we are able to discern cloud and cluster morphological information. The molecular structures detected in our CO survey (Chapter 2) are, on a qualitative level, clearly "seen" on our images as areas of enhanced extinction in comparison to the Galactic background. On a qualitative level, we can generalize the apparent radial distribution of stars with distance from the Ae/Be stars. At large radii, source counts are dominated by Galactic background / foreground stars. At smaller radii, the effects of cloud extinction can be seen, as stellar surface densities decrease with decreasing radial distance. At smaller radii still, source counts begin to increase with decreasing radial distance due to the presence of small stellar clusters near the centers of the frames, *i. e.* , near the Ae/Be stars. Close examination of the data frames leads us to the result that the Ae/Be stars are not forming in total isolation within their cloud cores. In

all cases at least several faint companions, and in some cases small clusters of sources, are also projected onto the molecular clouds. Many of these faint objects have the appearance of so-called "socket-stars."

The initial suspicion from our deep optical images of source clustering in the immediate vicinity of Ae/Be stars is enhanced by examination of our infrared images. These data frames (typically only 2-5 arcmin on a side) are smaller than the optical data frames (23 arcmin on a side). Thus, while they do penetrate the cloud cores to significantly greater depths (as discussed quantitatively above), the infrared frames are insufficient in spatial coverage for probing the radial distributions of source counts in a manner parallel to the manner in which we have described the optical frames. In general, over the small field sizes covered by the infrared frames, the number of companion stars is significantly higher than what we can discern from the optical frames. These stars may represent either physically associated core members which are more deeply embedded in the cloud than the surface populations, or background stars (in some cases) which are seen through low-extinction lines of sight.

The molecular data presented in Chapter 2 allowed us to confirm the association of Ae/Be stars with molecular gas. However, we found the local cloud environments typically to appear disturbed in some manner, although we cannot say at the present time whether this is due to dynamical processes external to the cloud or due to the interaction of the Ae/Be star itself with the cloud. Interestingly it may in fact be the disruption of the parent molecular cloud by the formation of a massive star which allows us to "see" any accompanying stellar population, well before we might otherwise in star-forming environments producing only less massive stars.

3.4 Conclusions from the Imaging Survey

We have described the parameters of a deep optical and infrared imaging survey over fields centered on young, massive, isolated Ae/Be stars. There is a suggestion from these images of stellar clustering (diagnosed via radial source count profiles on optical images and visual inspection of infrared images) within the boundaries of the dark insterstellar clouds with which the Ae/Be stars are associated. In order to further investigate the nature of the members of these newly discovered aggregates, we conducted an optical spectroscopic survey of the Ae/Be cores which we describe in the next Chapter. Then, in the remainder of this thesis, we analyze the clustering trends and the properties of the stellar populations.